

Atomic-scale structure characteristics of antiferroelectric silver niobate

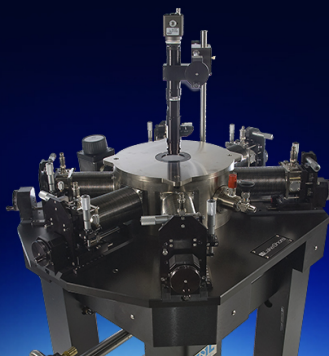
Gen Li, Hai Liu, Lei Zhao, Jing Gao, Jingfeng Li, Rong Yu, and Jing Zhu

Citation: *Appl. Phys. Lett.* **113**, 242901 (2018); doi: 10.1063/1.5061749

View online: <https://doi.org/10.1063/1.5061749>

View Table of Contents: <http://aip.scitation.org/toc/apl/113/24>

Published by the [American Institute of Physics](#)



Cryogenic probe stations
for accurate, repeatable
material measurements

LEARN MORE 

Atomic-scale structure characteristics of antiferroelectric silver niobate

Gen Li,¹ Hai Liu,¹ Lei Zhao,² Jing Gao,² Jingfeng Li,² Rong Yu,^{1,2} and Jing Zhu^{1,2,a)}

¹National Center for Electron Microscopy in Beijing, School of Materials Science and Engineering, The State Key Laboratory of New Ceramics and Fine Processing, Key Laboratory of Advanced Materials (MOE), Tsinghua University, Beijing 100084, People's Republic of China

²School of Materials Science and Engineering, The State Key Laboratory of New Ceramics and Fine Processing, Tsinghua University, Beijing 100084, People's Republic of China

(Received 23 September 2018; accepted 26 November 2018; published online 10 December 2018)

Antiferroelectric materials are a kind of functional material, which are widely used in electrostatic energy storage, energy conversion devices, and magnetoelectric coupling devices. As a typical lead-free antiferroelectric material, silver niobate has attracted much attention in recent years due to its excellent performance in energy storage. In this work, using the spherical aberration corrected electron microscopy technique, atomic-resolution images of pure silver niobate were obtained, which revealed typical microscopic physical characteristics of such complex antiferroelectric oxides: in such materials, all cations deviate from the average positions of the main lattice, and the displacement of each kind of cation varies periodically in two opposite directions, resulting in periodic wavy (1–10) \times atomic planes, and the period of cation displacement is 15.6 Å. At the same time, the 90° antiferroelectric domain boundary and the antiphase domain wall defects are further revealed and analyzed. *Published by AIP Publishing.* <https://doi.org/10.1063/1.5061749>

Antiferroelectric materials are an important class of functional materials. Compared to ferroelectric materials, the unit cell of an antiferroelectric material contains at least two localized electric dipoles with opposite directions, making the net polarization zero. Under a weak external electric field, its polarization is approximately proportional to the external electric field, while under a strong external electric field, the antiferroelectric-ferroelectric phase transition will occur. Therefore, the P-E loop of the antiferroelectric material usually appears as double hysteresis.

The antiferroelectric-ferroelectric phase transition of antiferroelectric materials belongs to structural phase transition with relatively large strain, which can be used in antiferroelectric-ferromagnetic heterojunctions.^{1–4} With the help of antiferroelectric materials, researchers can control the coercive magnetic field,³ the direction,⁴ and the value of the magnetic moment⁵ by adjusting the external electric field; and its inverse effect, namely, controlling the polarization and the strain of antiferroelectrics via the external magnetic field has also been realized,⁵ and the antiferroelectric phase can even be adjusted to the ferroelectric phase.⁶ In engineering applications, the large strain of antiferroelectric materials makes them suitable to be used in actuators in microelectromechanical systems.^{7,8} Furthermore, some antiferroelectric materials are also good piezoelectric materials. For instance, Sm-doped BiFeO₃ has outstanding piezoelectric properties near the morphotropic phase boundary and has great potential to be widely applied as a piezoelectric material.⁹

But, compared with all the above applications, antiferroelectric materials are more widely used in the electrostatic energy storage field. For antiferroelectric materials with double hysteresis loop, the energy storage density can be roughly written as the product of saturated polarization P_m and critical

electric field E_A . For most antiferroelectrics with a perovskite structure, the difference in the saturation polarization P_m is moderate, while the values of the critical field E_A vary widely. The most widely studied antiferroelectric energy storage materials are lead zirconate (PbZrO₃, PZO)¹⁰ and its doped products, such as strontium-doped lead zirconate (Pb_{1-x}Sr_xZrO₃, PSZ),¹¹ lanthanum-doped lead zirconate,¹² europium-doped lead zirconate,¹³ $\{(\text{Pb}_{0.97}\text{La}_{0.02})(\text{Zr}_{1-x-y}\text{Sn}_x\text{Ti}_y)\text{O}_3\}$,^{14–16} and $\text{Pb}_{0.99}\text{Nb}_{0.02}[(\text{Zr}_{0.57}\text{Sn}_{0.43})_{1-y}\text{Ti}_y]_{0.98}\text{O}_3\}$.¹⁷ Most of them have large E_A values and high energy storage densities. For example, the energy storage density of 3 mol. % Eu-doped lead zirconate can reach 18.8 J/cm³.¹³ However, all these antiferroelectric materials contain lead, which may cause great pollution. Therefore, researchers hope to realize high energy storage density in lead-free systems, and silver niobate is a candidate with high expectation.

Silver niobate possesses a perovskite structure. Both silver atoms in the A-site and niobium atoms in the B-site deviate along two opposite $\pm[110]_c$ directions, which break the lattice translational symmetry along the $[001]_c$ perpendicular to it, making the lattice constant along $[001]_c$ extend four times of the original one.¹⁸ Silver niobate has been synthesized in the 1950s,¹⁹ and the following research is mainly focused on analyzing its structure and phase transitions.^{20–29} After entering the 21st century, some researchers tried to analyze it using first-principles calculations.^{30–33} In summary, the anti-ferroelectric phase Pbcm and the ferroelectric phase Pmc2₁ exist simultaneously in a silver niobate system below 340 K; between 340 K and 626 K, there is an antiferroelectric phase Pbcm; and above 626 K, there are several paraelectric phases, namely, the orthorhombic Cmc2₁ phase, the tetragonal phase P4/mbm, and the cubic phase Pm $\bar{3}$ m, which appear in turn as temperature rises.

In 2007, Fu *et al.* reported that they found a polarization which registered at up to 52 $\mu\text{C}/\text{cm}^2$ in silver niobate polycrystals, and its P-E loop behaved like a double hysteresis

^{a)} Author to whom correspondence should be addressed: jzhu@mails.tsinghua.edu.cn, Tel.: +86 010-62794026

loop.²⁶ This led to an upsurge of research on the performance of silver niobate. In recent years, several breakthroughs were made in this system and attracted a lot of attention. In 2016, Tian *et al.* realized an energy storage density of 2.1 J/cm^3 in pure silver niobate,³⁴ and researchers began to further improve its energy storage density by doping. When doped with Mn, W, and Bi, the corresponding energy storage density could achieve 2.5 J/cm^3 , 3.0 J/cm^3 , and 3.3 J/cm^3 .^{35–37} In 2017, a large breakthrough was made by Zhao *et al.*, who improved the energy storage density to 4.2 J/cm^3 using Ta as the doping element.³⁸

Up to now, researchers have done a lot of work on antiferroelectric materials on a mesoscopic scale, but despite the maturity of microstructure analysis of ferroelectrics, the atomic-scale research of antiferroelectric materials is still barely seen. In this work, atomic-resolution high angle annular dark field (HAADF) images of antiferroelectric silver niobate were obtained, which revealed typical microscopic physical characteristics of such complex antiferroelectric oxides. The 90° antiferroelectric domain boundary and the antiphase domain wall defects are further reported and analyzed. These results will enhance the understanding of antiferroelectric materials such as silver niobate and bring inspiration for designing new antiferroelectric energy storage materials.

AgNbO_3 ceramics were prepared by a conventional solid-state reaction method using Ag_2O ($\geq 99.7\%$) and Nb_2O_5 ($\geq 99.99\%$) powders as the raw materials. These oxide powders were mixed using a planetary ball mill with anhydrous ethanol at 250 rpm for 24 h, in a nylon jar with zirconia ball media. The dried powder mixture was pressed into disks of 20 mm in diameter and 2 mm in thickness, and calcined at 900°C for 6 h in an O_2 atmosphere. The calcined powders were milled again and pressed into disks of 8 mm in diameter and 1.2 mm in thickness, followed by cold isostatic pressing under 220 MPa for 1.5 min. After that, samples were sintered at 1100°C for 6 h in an O_2 atmosphere to prevent the possible decomposition of silver oxide at high temperatures.

Conventional TEM investigations were performed using a FEI TECNAI G²20 TEM with a double tilting stage, operating at 200 kV. High resolution scanning transmission electron microscopy (HRSTEM) experiments were performed using a spherical aberration-corrected Titan Themis TEM with a double tilting stage, operating at 300 kV, and the STEM detector was a high angle annular dark field (HAADF) detector, with a camera length of 115 mm and the corresponding collection semi-angle range is $48\text{--}200 \text{ mrad}$. Samples for TEM experiments were first mechanically polished to $30 \mu\text{m}$. After that, a pit meter was used to grind a curved pit on the sample surface. The thickness of the pit bottom is about $10 \mu\text{m}$. Then, samples were ion-milled to reach electron transparency with a Gatan PIPS 695 system, in which Ar-ion beams operated at $0.1\text{--}4 \text{ kV}$. Using MacTempas software, the diffraction patterns of silver niobate crystals were simulated. All the image filtering, peak finding, Gaussian fitting and statistic work were performed using the self-made MATLAB code.

Previous investigations have shown that silver niobate has only two possible structures at room temperature: the

antiferroelectric Pbcm phase and the ferroelectric Pmc2₁ phase.^{21,22} Current research tends to believe that these two phases coexist at room temperature, but the Pmc2₁ phase occupies less volume fraction.^{26,34} The atomic structures of these two phases are very similar, and the only difference is that the Pbcm phase does not show any net macroscopic polarization, while the local polarizations in the Pmc2₁ phase cannot completely neutralize.¹⁸ The only way to separate these two phases in experiments is to perform selective area electron diffraction under a specific $[110]_c$ axis or perform Fourier transform on high resolution images.

With the help of spherical aberration correction technique, high resolution HAADF images of the pure Pbcm phase of the silver niobate sample under a pseudo-cubic $[110]_c$ zone axis were obtained, as shown in Fig. 1. In our experiments, the STEM fast scanning direction was perpendicular to the displacement direction of B-site atoms to minimize the drifting effect, making it reliable to analyze the atomic displacement between different horizontal rows.³⁹

Figure 1 shows the diffraction simulations and experimental images of pure silver niobate. Figures 1(c) and 1(d) show the simulated and experimental diffraction patterns of silver niobate with a Pbcm structure; Fig. 1(a) shows the HAADF image of pure silver niobate. The illustration in the upper right corner is its Fourier transform, which is consistent with Figs. 1(c) and 1(d), but different from the simulated diffraction pattern of the Pmc2₁ structure as shown in the [supplementary material](#), suggesting that the phase structure observed is Pbcm, but not the ferroelectric phase Pmc2₁. Typical atomic arrangement characteristics of antiferroelectric materials are shown in Fig. 1(a): each kind of cation deviates along two opposite directions and wavy atomic planes were formed. More specifically, silver and niobium atoms here exhibit displacement along the $\pm[1-10]_c$ direction, resulting in fluctuation along the $[001]_c$ direction: each successive four silver-niobium pairs form a repeating unit, which means that the fluctuation period has eight atoms, or 15.6 \AA , and the corresponding superlattice is $4a_c \times \sqrt{2}a_c \times \sqrt{2}a_c$. Such results are consistent with previous structural analysis given by X-ray diffraction and neutron diffraction.^{27,28} A crystal unit cell is illustrated with a colored image in Fig. 1(a), in which orange spots and green spots

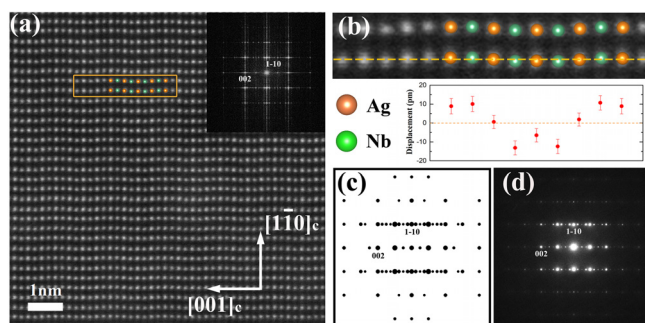


FIG. 1. The diffraction pattern and the HAADF image of the pure Pbcm phase of silver niobate. (a) The STEM-HAADF image of the pure Pbcm phase of silver niobate and the illustration in the upper right corner is its fast Fourier transform; (b) a magnified view of the orange rectangular area in (a), and the measured cation displacement values; (c) diffraction simulation of silver niobate of the Pbcm structure; and (d) the experimental diffraction pattern of the Pbcm phase of silver niobate.

stand for silver atoms and niobium atoms, respectively. This unit cell along with its surrounding area is magnified in Fig. 1(b), and the corresponding displacement values of cations were also measured and are shown. It can be seen that the maximum cation displacement is about 13 pm.

Similar to ferroelectric materials, there are also domain structures in antiferroelectric materials. Non-180° antiferroelectric domains are generally regarded as ferroelastic domains.⁴⁰ Using polarized light microscopy,^{41,42} transmission electron microscopy,^{43–47} laser confocal scanning microscopy,^{48–50} and piezoelectric power microscopy,⁵¹ researchers have already observed antiferroelectric domains in lead zirconate (PZO)^{41,46} and sodium niobate (NNO),^{47–50} and the polarization angles of adjacent antiferroelectric domains are mostly 90° and 60°.^{41,46,47} However, such works only analyzed materials in a meso-scale but did not reveal the atomic-scale characteristics of antiferroelectric domain boundaries.

Figure 2(a) shows a typical 90° antiferroelectric domain boundary in silver niobate. Here, the domain boundary is shown using a yellow dashed line. The microstructures in the left and right are quite different, and the domain boundary is not straight but formed by successive kinked (001)_c and (110)_c [or (−110)_c] planes. On the left side, atoms are arranged straight along the [001]_c direction; while on the right side, atoms along the [001]_c direction exhibit a wave-like arrangement as shown in Fig. 1(a). It can be seen more clearly in Fig. 2(b), which is a magnified view of the orange rectangular area in Fig. 2(a).

This phenomenon can be explained by the 90° antiferroelectric domain boundary: in the silver niobate crystal, the atomic antiferroelectric displacement appears only in $\pm[1-10]_c$ directions, and along other directions such as $[110]_c$

atoms arrange regularly. On the right side of Fig. 2(a), the incident direction of the electron beam is $[110]_c$ and obvious antiferroelectric displacement can be seen. However, with respect to the right-side lattice, the left-side lattice rotates 90° along the $[001]_c$ axis, which makes the real incident axis of the electron beam on the left side to be $[-110]_c$. In this situation, antiferroelectric displacement directions and the incident direction are colinear, making the antiferroelectric displacement invisible on the left-side.

The explanation above can be shown more directly in Fig. 2(c), which is a schematic three-dimensional structure of the area shown in Fig. 2(a). In Fig. 2(c), the orange cuboid represents the left-side lattice in Fig. 2(a) and the blue cuboid represents the right-side lattice. The red arrows in pairs stand for directions of local antiferroelectric displacement, or local electric dipoles. The antiferroelectric displacement directions are perpendicular to the electron beam in a blue cuboid but colinear with the electron beam in orange the cuboid, because the orange cuboid twists 90° along the $[001]_c$ axis with respect to the blue one. Therefore, the atomic antiferroelectric displacement cannot be seen in the corresponding projection plane.

In addition to the antiferroelectric domain boundary mentioned above, there are other types of defects in silver niobate. Figure 3 presents one typical defect structure in silver niobate. It is easy to find that there are transition areas with blurred lattice structures between region I and region II, and between region II and region III. There is a $[110]_c/4$ misalignment between adjacent lattice regions: the orange dashed line 1 lies between the atomic rows of region I and region III and covers the atoms in region II; while the blue dashed line 2 covers the atomic rows of region I and region III, but lies between atomic rows of region II. Such defects could be speculated as antiphase domain walls.

In conclusion, in this work, the atomic-resolution images of the antiferroelectric Pbcm phase of silver niobate were obtained with the help of a spherical aberration corrected technique, and typical microscopic physical characteristics of such complex antiferroelectric oxides were revealed: each kind of cation deviates along two opposite $\pm[1-10]_c$ directions and such an atomic arrangement eventually forms wavy (1-10)_c atomic planes. There are two main defects in such material. The first one is the 90° antiferroelectric domain boundary, which is formed by successive kinked (001)_c and (110)_c [or (−110)_c] planes, and the atomic column projections

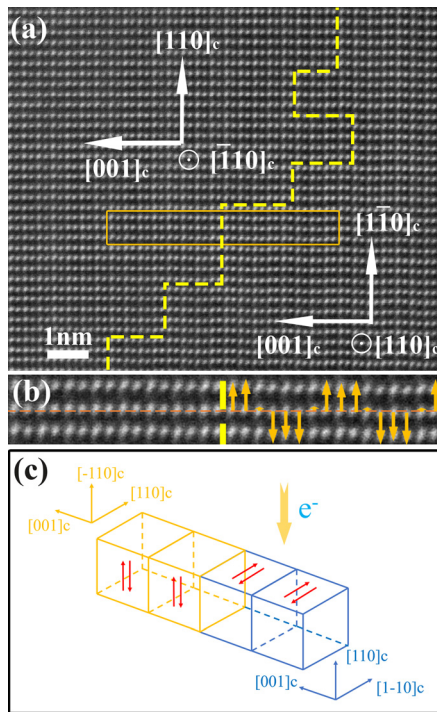


FIG. 2. The 90° antiferroelectric domain boundary in silver niobate. (a) A high-resolution HAADF image of the region near the domain boundary; (b) a magnified view of the orange rectangular area in (a), and local cation displacement directions are shown by orange arrows; (c) the schematic three-dimensional structure of the region near the domain boundary.

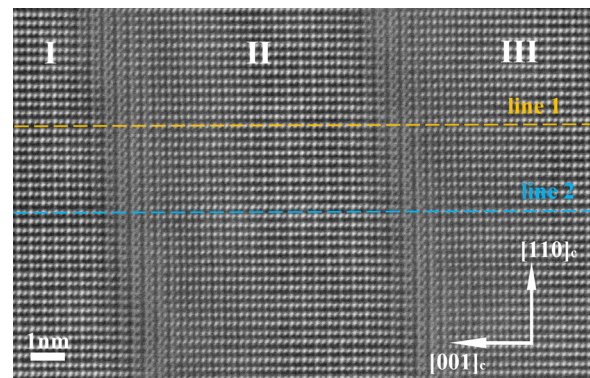


FIG. 3. The antiphase domain wall in silver niobate.

on both sides of the domain boundary have different arrangements. The other defect is the antiphase domain wall, in which the lattices on both sides have a misalignment of $[110]/4$. These results will be helpful for enhancing the understanding of the antiferroelectric mechanism of materials such as silver niobate and may provide guidance for designing new antiferroelectric energy storage materials.

See [supplementary material](#) for the STEM-ABF image of the Pbcm phase of silver niobate with the schematic unit cell containing oxygen atoms and a detailed explanation of how to confirm that the structure of silver niobate observed in the experiment is indeed the Pbcm phase.

This work was financially supported by the Chinese National Natural Science Foundation (51390471, 51527803, and 51761135131), the National 973 Project of China (2015CB654902), and the National Key Research and Development Program (2016YFB0700402). This work made use of the resources of the National Center for Electron Microscopy in Beijing.

- ¹N. X. Sun and G. Srinivasan, *Spin* **2**(3), 1240004 (2012).
- ²J. M. Liu, K. F. Wang, Y. Wang, Q. C. Li, and X. S. Gao, *Comput. Mater. Sci.* **30**(3-4), 389–396 (2004).
- ³Z. Zhou, X. Y. Zhang, T. F. Xie, T. X. Nan, Y. Gao, X. Yang, X. J. Wang, X. Y. He, P. S. Qiu, N. X. Sun, and D. Z. Sun, *Appl. Phys. Lett.* **104**, 012905 (2014).
- ⁴M. S. Mirshekarloo, N. Yakovlev, M. F. Wong, K. Yao, T. Sritharan, and C. S. Bhatia, *Appl. Phys. Lett.* **101**, 172905 (2012).
- ⁵J. P. Zhou, X. Z. Chen, L. Lv, C. Liu, and P. Liu, *Appl. Phys. A* **104**, 461–464 (2011).
- ⁶M. S. Mirshekarloo, K. Yao, and T. Sritharan, *Adv. Funct. Mater.* **22**(19), 4159–4164 (2012).
- ⁷W. P. Pan, Q. M. Zhang, A. Bhalla, and L. E. Cross, *J. Am. Ceram. Soc.* **72**(4), 571–578 (1989).
- ⁸M. S. Mirshekarloo, L. Zhang, K. Yao, and T. Sritharan, *Sens. Actuators A* **187**, 127–131 (2012).
- ⁹Z. Y. Liao, F. Xue, W. Sun, D. S. Song, Q. Q. Zhang, J. F. Li, L. Q. Chen, and J. Zhu, *Phys. Rev. B* **95**, 21 (2017).
- ¹⁰S. S. N. Bharadwaja and S. B. Krupanidhi, *Mater. Sci. Eng., B* **78**, 1–10 (2000).
- ¹¹X. H. Hao, J. W. Zhai, and X. Yao, *J. Am. Ceram. Soc.* **92**(5), 1133–1135 (2009).
- ¹²J. Parui and S. B. Krupanidhi, *Appl. Phys. Lett.* **92**, 192901 (2008).
- ¹³M. Ye, Q. Sun, X. Q. Chen, Z. H. Jiang, and F. P. Wang, *J. Am. Ceram. Soc.* **94**(10), 3234–3236 (2011).
- ¹⁴M. S. Mirshekarloo, K. Yao, and T. Sritharan, *Appl. Phys. Lett.* **97**, 142902 (2010).
- ¹⁵B. M. Xu, P. Moses, N. G. Pai, and L. E. Cross, *Appl. Phys. Lett.* **72**, 593 (1998).
- ¹⁶H. L. Zhang, X. F. Chen, F. Cao, G. S. Wang, and X. L. Dong, *J. Am. Ceram. Soc.* **93**(12), 4015–4017 (2010).
- ¹⁷S. E. Young, J. Y. Zhang, W. Hong, and X. Tan, *J. Appl. Phys.* **113**, 054101 (2013).
- ¹⁸M. Yashima, S. Matsuyama, R. Sano, M. Itoh, K. Tsuda, and D. S. Fu, *Chem. Mater.* **23**(7), 1643–1645 (2011).
- ¹⁹M. H. Francombe and B. Lewis, *Acta Crystallogr.* **11**(3), 175–178 (1958).
- ²⁰A. Kania, K. Roleder, and M. Łukaszewski, *Ferroelectrics* **52**(1), 265–269 (1984).
- ²¹M. Verwerft, G. V. Tendeloo, J. V. Landuyt, W. Coene, and S. Amelinckx, *Phys. Status Solidi A* **109**(62), 67–78 (1988).
- ²²M. Verwerft, D. V. Dyck, V. A. M. Brabers, J. V. Landuyt, and S. Amelinckx, *Phys. Status Solidi A* **112**(451), 451–466 (1989).
- ²³A. Kania, *Ferroelectrics* **205**(1), 19–28 (1998).
- ²⁴J. Fábry, Z. Zikmund, A. Kania, and V. Petříček, *Acta Crystallogr., Sect. C: Cryst. Struct. Commun.* **56**(8), 916–918 (2000).
- ²⁵A. Ratuszna, J. Pawluk, and A. Kania, *Phase Transitions* **76**(6), 611–620 (2003).
- ²⁶D. S. Fu, M. Endo, H. Taniguchi, T. Taniyama, and M. Itoh, *Appl. Phys. Lett.* **90**, 252907 (2007).
- ²⁷P. Sciau, A. Kania, B. Dkhil, E. Suard, and A. Ratuszna, *J. Phys.: Condens. Matter* **16**, 2795–2810 (2004).
- ²⁸I. Levin, V. Krayzman, J. C. Woicik, J. Karapetrova, T. Proffen, M. G. Tucker, and I. M. Reaney, *Phys. Rev. B* **79**, 104113 (2009).
- ²⁹I. Levin, J. C. Woicik, A. Llobet, M. G. Tucker, V. Krayzman, J. Pokorny, and I. M. Reaney, *Chem. Mater.* **22**, 4987–4995 (2010).
- ³⁰I. Grinberg and A. M. Rappe, *AIP Conf. Proc.* **677**, 130–138 (2003).
- ³¹M. K. Niranjana and S. Asthana, *Solid State Commun.* **152**(17), 1707–1710 (2012).
- ³²H. Moriwake, C. A. J. Fisher, A. Kuwabara, and D. S. Fu, *Jpn. J. Appl. Phys. Part 1* **51**, 09LE02 (2012).
- ³³M. Yashima and S. Matsuyama, *J. Phys. Chem. C* **116**(47), 24902–24906 (2012).
- ³⁴Y. Tian, L. Jin, H. F. Zhang, Z. Xu, X. Y. Wei, E. D. Politova, S. Y. Stefanovich, N. V. Tarakina, I. Abrahams, and H. X. Yan, *J. Mater. Chem. A* **4**(44), 17279–17287 (2016).
- ³⁵L. Zhao, Q. Liu, S. J. Zhang, and J. F. Li, *J. Mater. Chem. C* **4**, 8380–8384 (2016).
- ³⁶Y. Tian, L. Jin, H. F. Zhang, Z. Xu, X. Y. Wei, G. Viola, I. Abrahams, and H. X. Yan, *J. Mater. Chem. A* **5**(33), 17525–17531 (2017).
- ³⁷L. Zhao, J. Gao, Q. Liu, S. J. Zhang, and J. F. Li, *ACS Appl. Mater. Interfaces* **10**, 819–826 (2018).
- ³⁸L. Zhao, Q. Liu, J. Gao, S. J. Zhang, and J. F. Li, *Adv. Mater.* **29**(31), 1701824 (2017).
- ³⁹C. Ophus, J. Ciston, and C. T. Nelson, *Ultramicroscopy* **162**, 1–9 (2016).
- ⁴⁰X. Tan, J. Frederick, C. Ma, E. Aulbach, M. Marsilius, W. Hong, T. Granzow, W. Jo, and J. Rödel, *Phys. Rev. B* **81**, 014103 (2010).
- ⁴¹F. Jona, G. Shirane, and R. Pepinsky, *Phys. Rev.* **97**, 6 (1955).
- ⁴²A. Sawada, Y. Mase, Y. Takagi, and M. Midorikawa, *J. Phys. Soc. Jpn.* **29**(4), 969–972 (1970).
- ⁴³H. Moritake, N. Shigeno, M. Ozaki, and K. Yoshino, *Liq. Cryst.* **14**(5), 1283–1293 (1993).
- ⁴⁴S. Anwar and N. P. Lalla, *J. Solid State Chem.* **181**(5), 997–1004 (2008).
- ⁴⁵D. Viehland, *Phys. Rev. B* **52**(2), 778–791 (1995).
- ⁴⁶M. Tanaka, R. Saito, and K. Tsuzuki, *Jpn. J. Appl. Phys.* **21**(2), 291–298 (1982).
- ⁴⁷J. Chen and D. Feng, *Phys. Status Solidi A* **109**(171), 171–185 (1988).
- ⁴⁸S. Yamazoe, H. Sakurai, T. Saito, and T. Wada, *Appl. Phys. Lett.* **96**, 092901 (2010).
- ⁴⁹S. Yamazoe, A. Kohori, H. Sakurai, Y. Kitanaka, Y. Noguchi, M. Miyayama, and T. Wada, *J. Appl. Phys.* **112**, 052007 (2012).
- ⁵⁰I. Fujii and T. Wada, *Jpn. J. Appl. Phys. Part 1* **55**, 10TA02 (2016).
- ⁵¹F. P. Zhuo, Q. Li, Y. M. Zhou, Y. J. Ji, Q. F. Yan, Y. L. Zhang, X. Q. Xi, X. C. Chu, and W. W. Cao, *Acta Mater.* **148**, 28–37 (2018).